eNeuro

Disorders of the Nervous System

Transient Oxygen-Glucose Deprivation Causes Region- and Cell Type-Dependent Functional Deficits in the Mouse Hippocampus *In Vitro*

Paul Grube,[1] Cedric Heuermann,[1] Andrei Rozov,[1,2] Martin Both,[1] Andreas Draguhn,[1] and Dimitri Hefter[1,3]

[1]Institute for Physiology and Pathophysiology, University of Heidelberg, Heidelberg 69120, Germany, [2]Federal Center of Brain Research and Neurotechnologies, Moscow 117997, Russia, and [3]RG Animal Models in Psychiatry, Central Institute of Mental Health, Mannheim 68159, Germany

Abstract

Neurons are highly vulnerable to conditions of hypoxia-ischemia (HI) such as stroke or transient ischemic attacks. Recovery of cognitive and behavioral functions requires re-emergence of coordinated network activity, which, in turn, relies on the well-orchestrated interaction of pyramidal cells (PYRs) and interneurons. We therefore modelled HI in the mouse hippocampus, a particularly vulnerable region showing marked loss of PYR and fast-spiking interneurons (FSIs) after hypoxic-ischemic insults. Transient oxygen-glucose deprivation (OGD) in *ex vivo* hippocampal slices led to a rapid loss of neuronal activity and spontaneous network oscillations (sharp wave-ripple complexes; SPW-Rs), and to the occurrence of a spreading depolarization. Following reperfusion, both SPW-R and neuronal spiking resumed, but FSI activity remained strongly reduced compared with PYR. Whole-cell recordings in CA1 PYR revealed, however, a similar reduction of both EPSCs and IPSCs, leaving inhibition-excitation (I/E) balance unaltered. At the network level, SPW-R incidence was strongly reduced and the remaining network events showed region-specific changes including reduced ripple energy in CA3 and increased ripple frequency in CA1. Together, our data show that transient hippocampal energy depletion results in severe functional alterations at the cellular and network level. While I/E balance is maintained, synaptic activity, interneuron spiking and coordinated network patterns remain reduced. Such alterations may be network-level correlates of cognitive and functional deficits after cerebral HI.

Key words: brain slices; hippocampus; hypoxia-ischemia; oxygen-glucose deprivation; parvalbumin interneurons; sharp wave-ripple oscillations

---

Significance Statement

Neurons can recover following transient hypoxia-ischemia (HI), which is crucial for the survival of brain tissue in the ischemic penumbra. Brain tissue recovered from stroke is characterized by aberrant network activity. Essential to fast network oscillations are fast-spiking interneurons (FSIs), which, due to their high energy demand, might be especially vulnerable to metabolic stress. Here, our data from murine hippocampal slices demonstrate impaired functional recovery of FSI after transient HI compared to pyramidal cells (PYRs). Concurrently, ripple oscillations re-emerge with reduced incidence and altered waveforms. Thus, the present study confirms increased functional vulnerability of hippocampal FSI to HI and reveals specific impairments of network activity.

Introduction

Hypoxic-ischemic conditions of the brain such as stroke are one of the leading causes of death and morbidity (GBD 2019 Diseases and Injuries Collaborators, 2020). While severe hypoxia-ischemia (HI), as in the ischemic core, leads to rapid necrotic cell death, mild metabolic distress, as present in the penumbra, causes functional deficits with or without subsequent delayed apoptotic cell death (Mattson et al., 2000; Broughton et al., 2009; Şekerdağ et al., 2018). The acute functional changes in hypoxic networks may determine long-term functional outcome when this tissue survives (Guggisberg et al., 2019). Still, little is known about short-term effects of such reversible HI events on single cell and network activity. Better understanding of these processes might help develop therapeutic or preventive interventions in transient ischemia and stroke.

A phenomenon commonly observed in the ischemic penumbra is the occurrence of one or more hypoxia-induced spreading depolarizations (HSDs; for a detailed review please refer to Somjen, 2001; Dreier, 2011). This event results from the complete breakdown of the membrane potential because of insufficient ATP-driven pump activity and entails a dramatic shift of ions, including a massive influx of calcium. Interestingly, neurons recover their membrane potential and ability to fire action potentials (APs) on timely re-oxygenation (Müller and Somjen, 2000; Hefter et al., 2016; Revah et al., 2019). It is suspected that HSD represents an additional insult, and it can be seen as a hallmark of HI-induced neuronal damage (Dreier, 2011).

Stroke patients oftentimes suffer from cognitive decline and memory deficits (Pendlebury and Rothwell, 2009). As the hippocampus is a pivotal region for learning and memory formation, and its CA1 area is highly vulnerable to HI (Schmidt-Kastner and Freund, 1991; Schmidt-Kastner, 2015), we conducted our study in this brain area. Hippocampal network architecture is largely preserved in acutely prepared brain slices from rodents, enabling studying its function in a reduced preparation without confounding systemic effects (Aitken and Schiff, 1986; Schurr and Rigor, 1989; Croning and Haddad, 1998; Hefter et al., 2016). One important pattern of hippocampal network activity are sharp wave-ripple complexes (SPW-Rs), comprising propagating waves of increased activity with superimposed high-frequency network oscillations ($\sim$200 Hz). These patterns are regarded as crucial for a range of behavioral and cognitive functions such as memory formation. SPW-Rs entrain neuronal APs with high temporal precision (Ylinen et al., 1995; Both et al., 2008), which may be an important prerequisite for transient, stable activation of place-encoding ensembles (Buzsáki and Draguhn, 2004; Buzsáki, 2015; Hainmueller and Bartos, 2018). SPW-Rs arise within the hippocampus from an interplay between excitatory pyramidal cells (PYRs) and inhibitory interneurons (Csicsvari et al., 1999; Nimmrich et al., 2005; Schönberger et al., 2014; Buzsáki, 2015). Of particular importance for such fast synchronization processes are fast-spiking parvalbumin+ interneurons (PV-IN; Ylinen et al., 1995). Importantly, these cells might be especially vulnerable to HI-induced functional loss and cell damage (Kann et al., 2014; Kann, 2016; Povysheva et al., 2019; Elzoheiry et al., 2020). At the network level, this may lead to decreased inhibition-excitation (I/E) ratio, disturbed activity patterns and altered coupling between cellular spikes and local field potential (LFP) oscillations.

In this study, we compared the activity of fast-spiking interneurons (FSIs) and PYRs during fast network oscillations (SPW-R). We employed a model of transient oxygen-glucose deprivation (OGD) and reperfusion in acute murine brain slices to simulate transient, mild HI. Our data from field potential, tetrode, and patch clamp recordings confirm the hypothesis that transient OGD leads to strongly reduced FSI activity in comparison to PYR. This coincided with a partial recovery of SPW-R.

Materials and Methods

Animals and tissue handling

All experiments were performed in accordance with Baden-Wurttemberg state law (licenses T100 and T01/19) and institutional guidelines. Wild-type (WT) C57BL/6 and mice, expressing tdTomato in PV-INs [B6-129P2-Pvalbtm1 (cre)Arbr/Uhg:B6-Gt(ROSA)-26Sortm14(CAG-tdTomato)Hze; below abbreviated as PV-tdTomato], obtained from Charles River Laboratories of both sexes were killed on postnatal day (P)60–P90. For this, the animals were deeply anesthetized using CO_2 and decapitated following loss of righting reflex. The head was immediately transferred into ice-cold artificial CSF (ACSF), and the brain was swiftly removed from the skull, trimmed, glued onto a cutting platform, and surrounded by cooled ACSF [2–6°C; saturated with 95% O_2/5% CO_2 (carbogen)]. Composition of ACSF was as follows: 124 mM NaCl, 3.0 mM KCl, 1.8 mM $MgSO_4$, 1.6 mM $CaCl_2$, 10 mM glucose, 1.25 mM NaH_2PO_4, and 26 mM $NaHCO_3$, pH 7.4. Horizontal slices were cut at 450 µm thickness using a Leica V1200s vibratome (Leica Microsystems). Three slices containing the ventral to mid portion of the hippocampus were then halved, so that each hemi-slice contained a complete horizontal section of the hippocampus, and transferred to a Haas-type interface chamber and left to recover for at least 2 h at 32–33°C while they were perfused with carbogen-saturated ACSF (flow rate 1.5–2 ml/min).

OGD

Baseline electrophysiological data were recorded as described below while slices were superfused with ACSF. Only slices spontaneously expressing SPW-R with amplitude $>$ 0.2 mV and incidence $>$1 Hz were chosen for

experiments. Of six hippocampal slices, a median of 2 [1.5; 2.5] slices was used from each animal. To model HI the perfusion was switched to an equimolar ACSF solution containing mannitol instead of glucose, saturated with an oxygen-free gas mixture of 95% N_2/5% CO_2. As soon as an HSD was observed in the LFP recording, perfusion was switched back to carbogen-ACSF.

Electrophysiological recordings
Tetrode recordings

LFP and single unit discharges were recorded with one to four tetrodes placed in the CA1 and CA3 PYR layers. The tetrodes were made of four twisted 12.5-μm-diameter tungsten wires (California Fine Wire) and connected to a DPA-2FX amplifier (NPI Electronics). Signals were amplified 100×, low-pass filtered at 10 kHz, high-pass filtered at 0.3 Hz, and digitized at 20 kHz for off-line analysis (1401 interface and Spike-2 data acquisition program; CED). In five slices, additional ACSF-filled glass microelectrodes (tip diameter, 2–4 μm) were used for DC recording. These signals were amplified 100× (EXT10–2FX amplifier; NPI Electronics) and digitized at 20 kHz. Data were continuously collected from baseline recording (20 min), during OGD (5–10 min) until 60 min after SD.

LFP recordings were analyzed using custom-written MATLAB routines, adapted from Hefter et al. (2016). Briefly, SPW-Rs were detected as local maxima in 10-x downsampled, <50-Hz lowpassed signal. Ripples were detected as local maxima in 10-x downsampled, 100- to 300-Hz bandpass-filtered signal. Ripple properties were analyzed using Morlet wavelet transformation of time windows starting 33 ms before and ending 67 ms after the peak of each SPW. Maximum power between 140 and 320 Hz was detected; the corresponding frequency was defined as the ripple frequency. Ripple energy was defined as the integral of values above 0.5 of maximal power in this frequency range. Tetrodes with a ripple energy <3 a. u. or with a frequency of SPW, carrying superimposed ripples, <0.2 Hz were deemed misplaced and excluded from further analysis.

Spike detection and sorting were performed using the Wave_clus program (Quiroga et al., 2004; Chaure et al., 2018) with parameters as shown in Extended Data Figure 1-1. The aim of the method is to attribute extracellular spikes to putative units based on the spike shape. Briefly, for spike detection the signal was bandpass filtered (300–3000 Hz) and thresholded based on the estimated standard deviation of the background noise. Then, wavelet transforms for the detected spikes were performed and a number of wavelet coefficients were automatically selected based on their deviation from normality. Based on these wavelet coefficients superparamagnetic clustering, a simulation of physical interactions of data points and their K-nearest neighbors, was performed, and the resulting clusters saved. Finally, these putative unit clusters were curated by the experimentalist in the Wave_clus GUI based on AP and autocorrelogram (AC) shape.

Units were further divided into putative PYRs and FSIs using four physiological parameters that have been shown to reliably distinguish these cell types (Sirota et al., 2008; English et al., 2017). For this, the K-Means algorithm was run on four z score normalized dimensions: log10 interspike interval (ISI) mode, log10 ISI median, burst percentage (defined as number of ISI <8 ms divided by number of all ISI × 100), and trough-to-right-peak latency. We expected at least three clusters, representing PYRs, FSIs, and at least one cluster containing other cell types. To find the optimal number of clusters, cluster quality was evaluated by the Calinski-Harabasz criterion. It exhibited a peak at 5 when testing between 3 and 15 clusters; thus, the number of clusters was set to 5 (Extended Data Fig. 1-2A,B). Subsequently, properties of clusters were used for the categorization of each cluster into PYR or FSI, respectively. One cluster exhibited the FSI phenotype (low ISI, high burst percentage); three clusters exhibited a PYR-like phenotype (slow firing, low burst percentage) and were merged; the remaining cluster displayed a partially bursting, partially slow-spiking phenotype, which could not be clearly classified as PYR or FSI and was assigned a third label (MIX). As both PYR and interneuron populations are known to be heterogenous, MIX likely represents various other cell classes including non-FSIs. As the focus of this study lies in the differentiation between PYR and FSI, the MIX group was excluded from the main analysis (Extended Data Fig. 1-2E–L).

Additionally, cumulative activity of all detected spikes in each recording was analyzed as multiunit activity (MUA).

The preferred ripple phase of a unit was defined as the 50th percentile of the unit-to-ripple-phase cross-correlogram. Firing precision was calculated from the width of the time window φ_{in} in °, within which the 25th to 75th percentiles of spikes on a ripple cycle occurs, as: phase specificity = $(360° – 2 \times \varphi_{in})/360°$. Thus, phase specificity ranges from 0, in case of an equal distribution of spikes on the ripple cycle ($\varphi_{in} = 180°$), to 1, if all spikes occur precisely in phase ($\varphi_{in} = 0°$).

Patch clamp recordings

Following OGD, some slices were left for 20 min of recovery time in the interface-chamber (which was sufficient for SPW-R to re-emerge) while control slices were maintained in the interface-chamber without OGD, matching incubation time of OGD slices. Then, they were quickly transferred to a submerged-style, double-sided perfusion chamber (Hájos et al., 2009; Maier et al., 2009) for patch-clamp recordings (carbogen-saturated ACSF at 6 ml/min, 32–33°C). Under these conditions, all slices retained spontaneous SPW-R activity. Field potentials in the stratum pyramidale of CA1 were recorded simultaneously to the patch clamp recordings, using ACSF-filled glass microelectrodes (tip diameter, 2–4 μm). These signals were amplified 100×, low-pass filtered at 2 kHz, high-pass filtered at 0.3 Hz (EXT10–2FX amplifier; NPI Electronics) and digitized at 20 kHz.

Whole-cell voltage-clamp recordings

In slices obtained from WT animals CA1 pyramidal neurons were visualized with a DIR microscope. To reduce variability, we chose neurons with the typical soma shape in the superficial layer of proximal CA1 (60×

magnification, BX51WI microscope, Olympus), as CA1 neurons have been shown to receive differential strengths of inhibition along the layers (Lee et al., 2014) and CA3–CA1 connectivity differs between the subregions of CA1 (Ishizuka et al., 1990). Whole-cell voltage-clamp recordings were performed with borosilicate electrodes (3–5 MΩ) filled with the following: 144 mM Cs-Gluc, 10 mM HEPES, 4 mM NaCl, 4 mM Mg-ATP, 0.3 mM Mg-GTP, and 10 mM phosphocreatine, pH 7.3, 1% Biocytin. Voltage signals were low-pass filtered at 8 kHz; current signals were low-pass filtered at 3 kHz (ELC-03XS amplifier; NPI Electronics) and both were digitized at 20 kHz. Pipette holding potential and offset were zeroed manually before seal formation. The liquid junction potential was calculated to be 15 mV and subtracted from the voltage data. Currents were recorded for 30 s each at −75-, −60-, 0-, and +15-mV nominal holding potential (corrected values: −90, −75, −15, and 0 mV). Access resistance and series resistance were monitored before and after each recording. Only cells with access resistance <30 MΩ and expressing a PYR-like electrophysiological phenotype were chosen; cells with an increase of series resistance >15% during the experiment were discarded.

Conductance changes during SPW-R events were analyzed through a custom MATLAB script based on a modification of the method by (Borg-Graham et al., 1998; Haider et al., 2006; Maier et al., 2016) to dissect inhibitory and excitatory conductance changes. Current traces (I_m), recorded at different holding voltages (V_h, listed above) during network events, were aligned by the peaks of individual SPW-R. Input conductance $G_{in}(t)$ was computed as the slope of the linear regression of the I–V relation between V_h and $I_m(t)$. The apparent reversal potential E_{arev} was taken from the intersection between $I_m(0)$ (during baseline before the SPW-R event) and $I_m(t)$ (during SPW-R-triggered postsynaptic events). The synaptic conductance change was calculated as $G_{chg}(t) = G_{in}(t) - G_{in}(0)$. AMPA and GABA reversal potentials were set to 0 mV (E_{AMPA}) and −90 mV (E_{GABA}), respectively. Inhibitory ($G_{chg, i}$) and excitatory ($G_{chg, e}$) conductance changes were then calculated as: $G_{chg, i} = G_{chg} \times (E_{arev} - E_{AMPA})/(E_{GABA} - E_{AMPA})$ and $G_{chg, e} = G_{chg} - G_{chg, i}$.

For analysis of spontaneous postsynaptic currents (sPSC), −75- and +15-mV nominal holding voltage was used. After correction by the liquid junction potential these values correspond to 0 mV [E_{rev} for spontaneous EPSCs (sEPSCs)] and −90 mV (E_{rev} for sIPSCs with 4 mM intracellular and ~130 mM extracellular [Cl⁻]). For analysis of these data, only SPW-R-free intervals were taken. Traces were bandpass-filtered (1–400 Hz for sEPSC; 1–200 Hz for sIPSC). A deconvolution-based algorithm was used to detect the PSCs. The deconvolution template comprised a double-exponential curve, resembling the physiological kinetics of recorded PSCs (Tauon of 1.25 ms, Tauoff of 3 ms for sEPSC; Tauon of 2.5 ms, Tauoff of 10 ms for sIPSC). PSCs were detected as local maxima in the deconvolved signal, combined with an amplitude threshold in the original signal as a secondary condition (>20 pA for sEPSC; >30 pA for sIPSC). Charge transfer of sPSC was defined as the integral within the

time window of [sPSC peak − Tauon; sPSC peak + Tauoff]. Total sPSC current for the analysis time was defined as charge × frequency. I/E ratio was defined as sIPSC current/sEPSC current.

Cell-attached recordings

PV-IN in PV-tdTomato mice were visualized by epifluorescence (60× magnification, BX51WI microscope, Olympus). Borosilicate electrodes (3–5 MΩ) were filled with ACSF and cell-attached recordings were performed from CA1 PV-IN according to (Perkins, 2006). After achieving a loose seal (<1 GΩ) configuration, APs were monitored in voltage-clamp mode with the voltage manually set such that the measured holding current equaled zero. APs were then visible as brief deflections in the current trace. Throughout the article, we refer to this configuration as "cell-attached." Current and LFP were recorded simultaneously for 200 s. A single threshold was used after offline bandpass filtering (100–5000 Hz) of recorded currents to determine spikes. Autocorrelations of spike times and their cross-correlations to LFP were calculated in MATLAB.

Histology

Directly after recording, ~1 h after HSD, slices were fixated in PFA for 12 h and thereafter stored in PBS at 4°C. Slices were then sub-sliced at 50 μm on a Leica V1200s vibratome (Leica Microsystems) and kept in a solution of v/v 31% ethylene glycol, 29% glycerin in PBS at −20°C until further processing. Slicing before experiments on living slices leads to damage and death of neurons close to the slice surface, and HI damage strongly correlates with depth within the tissue (Kann, 2012; Huchzermeyer et al., 2013). For these reasons, we chose two sub-slices from the middle portion of each original slice for staining.

We analyzed nuclear area and c-Fos co-expression by neuronal cell type. Sections were washed three times in PBS and blocked with 5% normal goat serum/0.3% Triton X-100 in PBS for 1 h. Thereafter, they were washed again in PBS and incubated with rabbit-anti-c-Fos (1:1000, Synaptic Systems), mouse-anti-PV (1:1000, Swant), and chicken-anti-NeuN (1:250, Synaptic Systems) primary antibodies in 1% normal goat serum/0.2% Triton X-100 in PBS for 18 h at room temperature. Upon washing with PBS, sections were incubated with Alexa Fluor 488 goat anti-rabbit (1:1000, Thermo Fisher Scientific), Cy3 goat anti-mouse (1:500, Dianova), Alexa Fluor 647 goat-anti-chicken (1:500, Thermo Fisher Scientific) secondary antibodies in 1% normal goat serum/0.2% Triton X-100 in PBS for 2 h at room temperature under light protection. Sections were then mounted onto slides with Fluoroshield (Sigma-Aldrich), containing DAPI, for nuclear staining. Fluorescence images were taken on a Nikon A1R (Nikon Instruments Inc.) confocal microscope system using a Nikon Plan Apo λ 20× NA 0.7 objective.

For image analysis, the experimentalist was blinded toward experimental conditions. Fluorescent images were preprocessed in Fiji ImageJ (Schindelin et al., 2012), as follows. First, regions of interest covering the stratum pyramidale and stratum oriens were selected for both CA1 and CA3, on which further processing and analysis were performed.

Fluorescence channels were split into separate grayscale images, and the background was removed employing a rolling-ball algorithm. Then, cells and nuclei were segmented automatically using the cellpose algorithm (Stringer et al., 2021) with settings "pretrained model nuclei" for the DAPI and c-Fos channels, and "pretrained model cyto" for the PV and NeuN channels. Co-expression of c-Fos and nuclear size were determined automatically in Fiji ImageJ through a custom script.

Statistical analyses

All statistical tests were performed in MATLAB. For statistical analyses of conductance changes, sPSC frequency and amplitude, and cell-attached spiking, we compared post-OGD to control groups. In the case of tetrode recordings, we performed within-group tests for the FSI and PYR groups, and for SPW-R parameters. Additionally, a between-group test for the relative frequency change of PYR compared with FSI was performed. The one-sample Kolmogorov–Smirnov test was used to test the normality of a given sample distribution. For normally distributed data, Student's two-sided t test was used to test for statistical significance of differences between two groups, and Student's paired sample t test for paired values. In case of non-normally distributed data, Wilcoxon's rank-sum test and Wilcoxon's signed-rank test were used for unpaired and paired data, respectively. For comparing the distributions of interevent intervals (IEIs) of sPSC between groups, the two-sample Kolmogorov–Smirnov test was used. For comparison of preferred ripple phase, the Watson–Williams test was used. The number n of experimental units, number of slices, and number of animals are indicated at the bottom of each figure legend. Null hypotheses were rejected at a significance level of $\alpha = 0.05$. Throughout the article, data are presented as median [25th; 75th percentiles], if not stated otherwise.

Results

Neuronal activity is reduced strongest among FSIs after transient hypoxia

We hypothesized that FSI activity might be more susceptible to hypoxia than that of PYRs. To test this, we measured unit activity from the hippocampal CA1 and CA3 regions with tetrodes before, during, and after transient OGD (Fig. 1A). Since FSI and PYR clearly differ in their respective firing pattern and AP waveform (Fig. 1A,B; Extended Data Fig. 1-2), we employed a clustering algorithm based on parameters reflecting these physiological properties (Extended Data Fig. 1-2) to differentiate between them. From 376 identified units, 26 units were classified as putative FSI and 296 units were clustered as putative PYR. The remaining 54 units did not fall into one of these classes and likely represent a mixed population of cells including bursting PYR and different types of interneurons (Klausberger and Somogyi, 2008).

Median baseline activity was 2.96 [0.81; 6.99] Hz for FSI and 1.10 [0.43; 2.37] Hz for PYR (Fig. 1E). In both groups, spiking was most pronounced during spontaneous SPW-R oscillations (Fig. 1B,F), consistent with previous findings (Both et al., 2008; Reichinnek et al., 2010). Switching to glucose-free and oxygen-free solution led to a spreading depolarization (SD) in all slices with delay times of 5.58 [4.25; 10.16] min ($n = 25$). The SD was characterized by a large negative deflection in the LFP, accompanied by a drastic reduction of unit activity in the LFP (Fig. 1A, representative trace; Extended Data Fig. 1-3A–C; please refer to Somjen, 2001; Dreier, 2011) for a review of SD mechanisms). Following reperfusion, most (>95%) of the previously identified units resumed activity, excluding acute cell death, as network events slowly re-emerged (Fig. 5B–E), reaching stable conditions 40–60 min after reperfusion (Fig. 1C,D).

FSI spiking showed a reduced recovery as compared with PYR throughout the whole time course of reperfusion (Fig. 1C, note difference between median recovery of FSI vs PYR). After 1 h, median activity of FSI reached only ∼36% of baseline values, in contrast to ∼64% in PYR (Fig. 1C). All putative FSI displayed lower firing rates after recovery from OGD, while the recovery of PYR was more diverse (Fig. 1D). Notably, some PYR regained higher activity rates than before OGD while all FSI showed values below the baseline situation. Still, median frequency was reduced significantly in both FSI and PYR (Fig. 1E). Firing during SPW-Rs was slightly reduced in both groups (Fig. 1F). Importantly, FSI frequency decreased significantly stronger than PYR frequency, as shown by the relative frequency change index, −0.43 [−0.83; −0.24] in FSI compared with −0.26 [−0.55; 0.07] in PYR (Fig. 1G, $p = 0.003$). Remarkably, these changes in unit firing did not correlate with the latency to HSD (Extended Data Fig. 1-3D,E).

Coupling precision of units to SPW-R is preserved

Inhibitory interneurons play a critical role in the temporal organization of network activity. We therefore tested whether the observed effects of transient OGD disrupted the timing of neuronal discharges. Under baseline conditions, averaged, normalized spike ACs mirror the fast-spiking phenotype of FSI while PYR AC are of much lower amplitude, indicating that PYR fire less frequently during individual SPW-R events (Fig. 2A,B; for further analysis of FSI and PYR properties, refer to Extended Data Fig. 1-2E–L). Note that peaks in both FSI and PYR AC at ∼5 ms reflect the recorded ripple frequency (∼200 Hz). Interestingly, the overall shape of the AC appeared similar after recovery from OGD in both types of neurons, indicating preserved coupling to sharp waves and ripple oscillations (compare Fig. 2A and C). The specificity of FSI and PYR spiking during SPW-R periods, i.e., the relative sparseness of firing outside network events, increased slightly following OGD (Fig. 2D). Preferred ripple phases of firing for both FSI and PYR spikes did not change significantly (Fig. 2E,F). Similarly, firing precision, measured as ripple phase specificity (for more details, see Materials and Methods, Tetrode recordings) also remained high in both FSI and PYR (Fig. 2G). In summary, unit activity of FSIs and PYRs
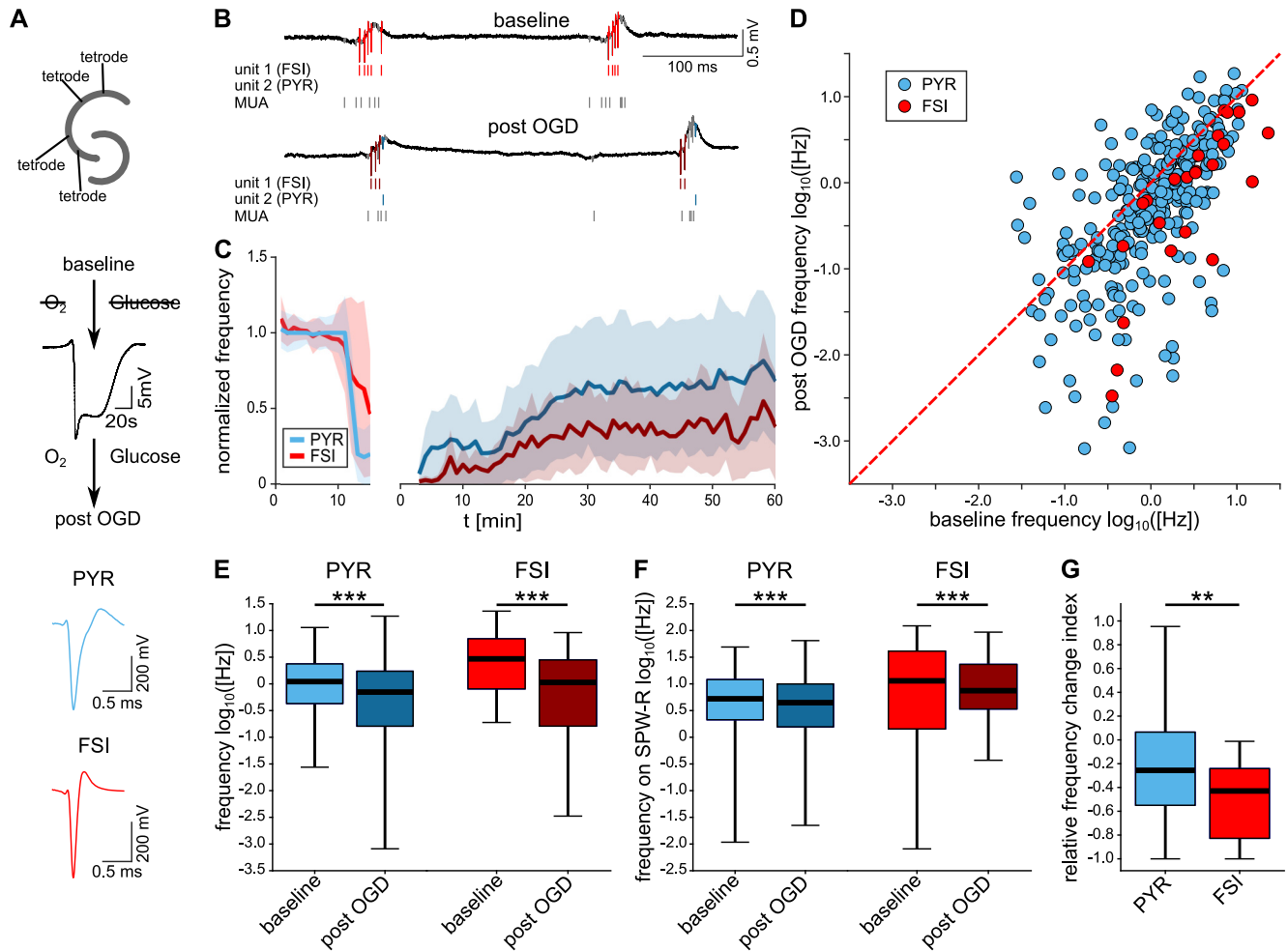
Figure 1. Firing of FSIs is reduced more strongly than PYR firing after OGD and recovery. ***A***, Experimental design. Top, Two tetrodes in each CA3 and CA1 regions of the hippocampal slice in an interface chamber. Middle, For OGD, perfusion was switched to an oxygen-glucose-free medium, until a HSD occurred (see representative LFP trace), whereupon perfusion was switched back to oxygenated ACSF. Bottom, Mean waveforms are shown for one putative FSI and one PYR. ***B***, Exemplary LFP recorded by tetrodes during baseline (top) and after recovery from OGD (bottom). Spike times of one FSI (red overlay), one PYR (blue overlay), and other units (MUA, gray overlay) are highlighted. ***C***, Binned median frequency of PYR (blue) and FSI (red), normalized by the median baseline frequency. Shaded regions represent the median absolute deviation. Minutes 0–10, baseline condition; minutes 10–15, OGD. Gap, HSD (because of variable latency from OGD onset to the occurrence of HSD in each experiment). Traces after gap, recovery during reperfusion. Time count on the right part of the x-axis begins with the time point of the HSD. ***D***, Logarithmic scatter plot of spiking frequencies of each unit, baseline (x-axis) compared with after 40–60 min of reperfusion (y-axis). Blue, PYR; red, FSI. ***E***, Unit spiking frequency during baseline and after recovery. $p_{PYR} = 3 \times 10^{-8}$. $p_{FSI} = 8 \times 10^{-6}$, Wilcoxon signed-rank test. ***F***, Frequency of unit spiking on SPW-R during baseline and after recovery. $p_{PYR} = 0.0003$. $p_{FSI} = 0.0006$, Wilcoxon signed-rank test. ***G***, Relative frequency change index, calculated as ($f_{post-OGD} - f_{baseline}$)/($f_{post-OGD} + f_{baseline}$). $p = 0.0028$, Student's t test. $n_{PYR} = 296$ units, $n_{FSI} = 26$ units from 25 slices, 12 mice; **$p < 0.01$, ***$p < 0.001$. Please refer to Extended Data Figure 1-1 for the parameters used in the spike sorting algorithm, Extended Data Figure 1-2 for the clustering of units into FSI and PYR, and Extended Data Figure 1-3 for the properties of the HSD.

recovers its temporal coupling to SPW-R network activity after transient OGD.

PV-INs display reduced spiking after recovery from OGD

To validate the findings from tetrode recordings, we performed cell-attached recordings from CA1 PV-INs together with LFP recordings (Fig. 3A–C). Measurements were performed in a submerged chamber on five (control) and four (post-OGD) slices from the same three mice where PV-IN could be identified by their tdTomato fluorescence

(Fig. 3A,B; see Materials and Methods, Cell-attached recordings). We compared slices after OGD/HSD and recovery with controls incubated in normal ACSF.

Following transfer from the interface-type to the submerged-type chamber, all slices from both the control and post-OGD group displayed spontaneous SPW-R events in the LFP (Fig. 3C, representative trace). In cell-attached recordings all PV-IN fired spontaneous APs which were strongly coupled to SPW-R (Fig. 3D). In line with the findings from tetrode recordings, the median spiking frequency of PV-IN in the post-OGD group was ~60% lower
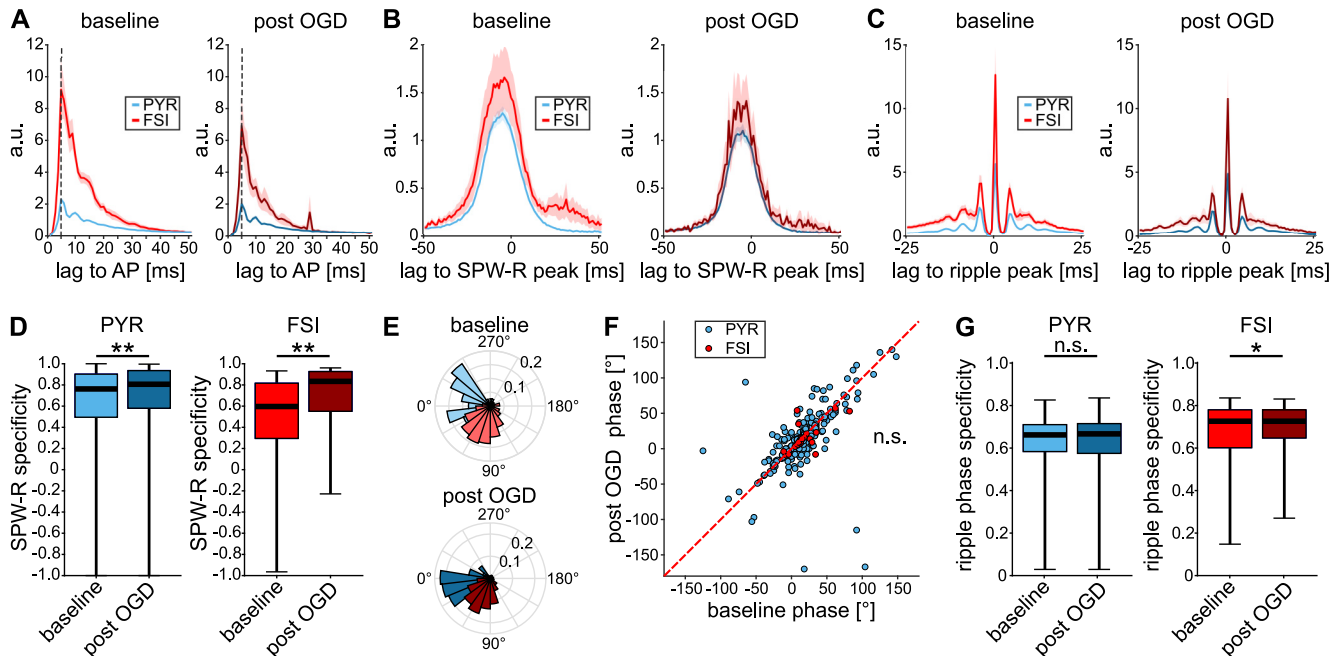
Figure 2. Coupling between unit firing and underlying network events recovers. ***A***, Mean autocorrelation of FSI (red) and PYR (blue) spike times. Dashed lines mark the first peak of the autocorrelation at 5 ms. ***B***, Mean cross-correlation between SPW-R peaks and FSI (red) or PYR (blue) spike times. ***C***, Mean cross-correlation between ripple peaks and FSI (red) or PYR (blue) spike times. In ***A–C***, shaded regions represent the SEM. Correlations were normalized, as follows: $n_{norm} = n_{corr}/\mathrm{sqrt}(n_{ev1} \times n_{ev2})$. The count of events n_{corr} within the displayed time window was divided by the square root of the product of the total occurrence of the event n_{ev1} to which the other event n_{ev2} was correlated, times the total occurrence of n_{ev2}. ***D***, Specificity of spike times to SPW-R time frames, calculated as $(f_{inside} - f_{outside})/(f_{inside} + f_{outside})$, where a value of 1 corresponds to firing being restricted to SPW-R and a value of -1 to firing only outside SPW-R. $p_{PYR} = 0.0042$. $p_{FSI} = 0.0021$, Wilcoxon signed-rank test. ***E***, Representative phase plot of spiking of one representative PYR (blue) and one FSI (red) unit on ripples, normalized by spike probability. 0° equals to the trough of the ripple cycle. ***F***, Scatter plot of preferred ripple phase for each unit, baseline paired with post-OGD values. Blue, PYR. Red, FSI. $p_{PYR} = 0.904$. $p_{FSI} = 0.681$, Watson–Williams test. ***G***, Specificity of spiking to the preferred ripple phase. $p_{PYR} = 0.117$. $p_{FSI} = 0.012$, Wilcoxon signed-rank test. $n_{PYR} = 296$ units, $n_{FSI} = 26$ units from 25 slices, 12 mice; *$p < 0.05$, **$p < 0.01$; n.s., not significant.

than that of controls (2.05 [1.66; 2.71] Hz compared with 4.91 [3.37; 5.44] Hz; Fig. 3*E*, $p = 0.003$). Additionally, OGD-challenged PV-IN fired less APs per SPW-R than controls (Fig. 3*F*), consistent with the higher ISI (Fig. 3*G*). Nevertheless, both the OGD and the control group displayed peaks at ~5 ms in the averaged AC (Fig. 3*H*), corresponding to the ripple frequency and indicating preserved coupling to individual ripple cycles. Ripple oscillations in the LFP signal were, however, less pronounced under these experimental conditions, such that a cross-correlation analysis did not yield clear results. Firing outside of SPW-R remained low in the OGD group (Fig. 3*I*) and PV-IN spiked almost exclusively on SPW-R events, as shown by a specificity index close to 1 in both groups (Fig. 3*J*). Thus, cell-attached recorded PV-IN show a strong reduction of spiking frequency, yet preserved spike coupling to SPW-R, validating the findings from tetrode recordings.

Postsynaptic conductance changes during SPW-R are reduced

To test whether the observed preferential decrease in FSI spiking led to changes in I/E balance, we performed whole-cell patch clamp recordings from CA1 PYRs in both post-OGD and control slices (Fig. 4*A,B,D*). We recorded PSCs at different holding potentials from -75 to $+15$ mV and calculated inhibitory and excitatory conductance changes during SPW-R, using the method previously described (Borg-Graham et al., 1998; Fig. 4*C–G*). In line with previous studies, we observed that input to CA1 PYRs during SPW-R consisted predominantly of a large inhibitory conductance increase and a 4- to 5-fold smaller excitatory component (Fig. 4*E*).

Input resistance was similar in control and post-OGD neurons, 139.83 [129.19; 155.04] MΩ in the control group compared with 162.83 [118.72; 186.97] MΩ in the post-OGD group ($p = 0.4121$).

The amplitude of the inhibitory conductance changes during SPW-R was significantly smaller in the post-OGD group (8.1 [5.9; 10.8] nS) compared with the control group (12.5 [10.6; 15.2] nS; Fig. 4*F*; $p = 0.02$). Likewise, excitatory conductance changes during SPW-R were smaller in slices after OGD (2.2 [1.2; 2.6] nS) than in slices from control conditions (2.9 [2.2; 4.4] nS; Fig. 4*F*; $p = 0.03$). These similar changes resulted in unaltered ratios between inhibitory and excitatory conductance changes during SPW-R network events (Fig. 4*G*).

We furthermore evaluated sPSCs measured in-between SPW-R network events (Fig. 4*H–M*). Frequency and area
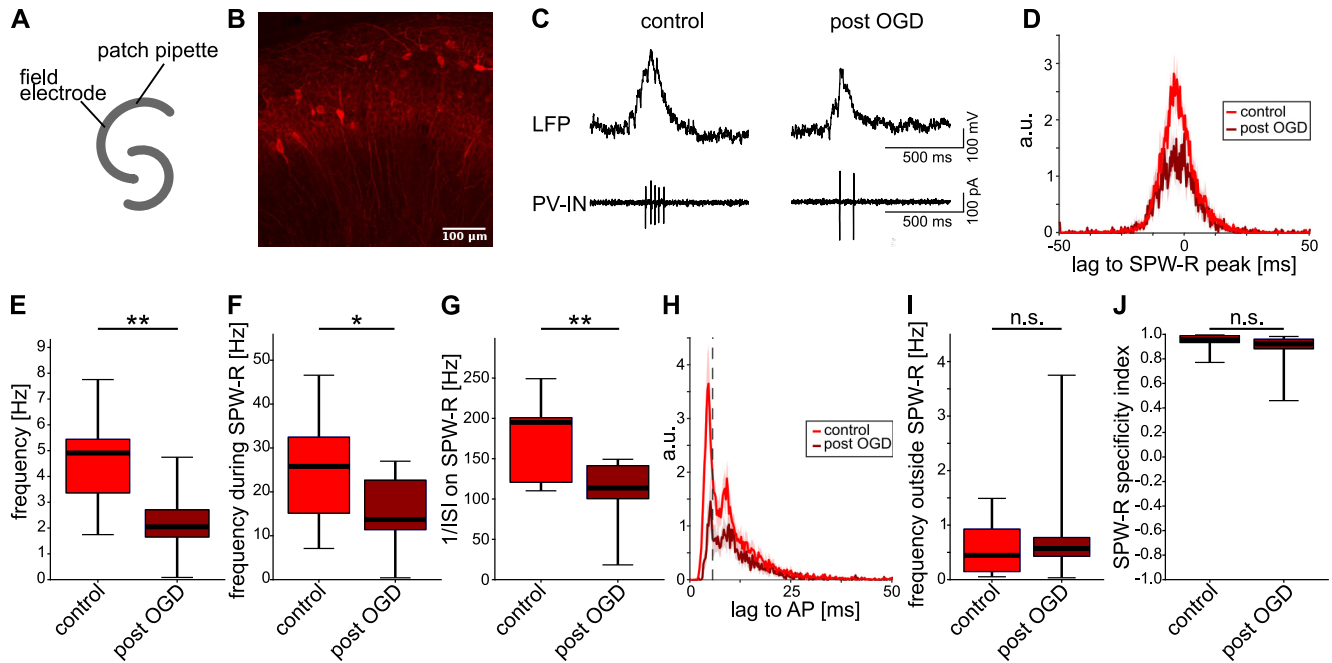
Figure 3. Cell-attached recordings reveal decreased spiking in CA1 PV-INs after transient OGD. ***A***, Experimental condition. A field electrode and a patch pipette were placed in the CA1 region of a hippocampal slice in a submerged chamber. ***B***, Representative image of the CA1 region in a horizontal slice from the PV-tdTomato mouse line at 20× magnification. ***C***, Representative traces. Top, SPW-R in the LFP. Bottom, PV-IN spikes recorded in the cell-attached voltage-clamp configuration simultaneously to the LFP recording. Left, Control recording. Right, Recording after OGD, HSD, and recovery. ***D***, Normalized mean cross-correlation between SPW-R peaks and spike times under control (red) and post-OGD (dark red) conditions. ***E***, Overall spike frequency. $p = 0.0026$. ***F***, Frequency during SPW-R-events. $p = 0.046$. ***G***, Instantaneous frequency (1/ISI) on SPW-R (if at least two spikes were detected during a SPW-R). $p = 0.0043$. ***H***, Normalized mean autocorrelation of spike times under control (red) and post-OGD (dark red) conditions. The dashed line marks the first peak of the autocorrelation at 5 ms. ***D***, ***H***, Shaded regions represent the SEM. Correlations were normalized, as follows: $n_{norm} = n_{corr}/\sqrt{(n_{ev1} \times n_{ev2})}$. ***I***, Frequency outside SPW-R. $p = 0.476$. ***J***, Specificity of spike times to SPW-R time frames, calculated as $(f_{inside} - f_{outside})/(f_{inside} + f_{outside})$. $p = 0.176$. $n_{control} = 12$ cells from 5 slices and 3 mice, $n_{post\text{-}OGD} = 10$ cells from 4 slices and the same 3 mice; *$p < 0.05$, **$p < 0.01$; n.s., not significant. Student's t test.

under the curve (AUC) of inhibitory and excitatory sPSCs were not significantly altered after transient hypoxia (Fig. 4H,I), despite an apparent trend toward decreased median sIPSC frequency. Cumulative distributions of IEIs displayed a significant shift of IEIs for sIPSC toward larger intervals, while sEPSC IEI were slightly shifted to shorter intervals (Fig. 4J,M). Amplitude distribution was unaltered between the two conditions for both sIPSC and sEPSC (Fig. 4J,M). Similar to synaptic conductances during SPW-R, the ratio of inhibitory to excitatory AUC outside SPW-R was not significantly reduced, despite some apparent trend to a relative decrease in inhibition (Fig. 4L).

Overall, following the recovery from OGD, no significant change in I/E ratio during or outside SPW-R was observed.

Network events recover partially

Fast, rhythmic inhibition is necessary for coordinated network activity. We hypothesized that deficits in fast inhibitory signaling might be accompanied by altered ripple oscillations. We therefore evaluated waveform parameters of extracellularly recorded SPW-R before, during, and after transient OGD (Fig. 5A).

In all slices, the LFP displayed spontaneous SPW-R activity, consisting of the slow, large amplitude sharp wave

occurring with an incidence of ~3 Hz and fast superimposed ripple oscillations (~220 Hz). OGD abolished SPW-R activity within 3–5 min. Following OGD, HSD, and re-oxygenation, SPW-R events re-emerged in all slices. Amplitude and frequency of the recovered events stabilized ~40 min after HSD (Fig. 5B,C). We compared SPW-R 40–60 min after HSD to baseline SPW-R.

Following OGD, a number of differences to baseline SPW-R were apparent. First, the incidence of SPW-R events was reduced from 3.03 [2.25; 3.56] Hz to 1.84 [1.23; 2.47] Hz in the CA1 region and from 2.94 [2.65; 3.24] Hz to 2.30 [1.69; 2.98] Hz in the CA3 region (Fig. 5D, E). In both regions, SPW-R incidence did not correlate with the latency to HSD (Extended Data Fig. 1-3F,G). Second, SPW-R amplitude was reduced in CA3 while it stayed unaltered in CA1 (Fig. 5D,E). Third, ripple parameters also displayed treatment-dependent and region-dependent differences. The frequency of ripple oscillations was increased in the CA1 region post-OGD, while it remained mostly unchanged in the CA3 region. Ripple energy was lower in CA3 with no clear change in the CA1 region (Fig. 5D,E).

To evaluate the coupling of unbiased, cumulative neural activity to SPW-R, we compared MUA during baseline and after recovery. As expected, baseline MUA was
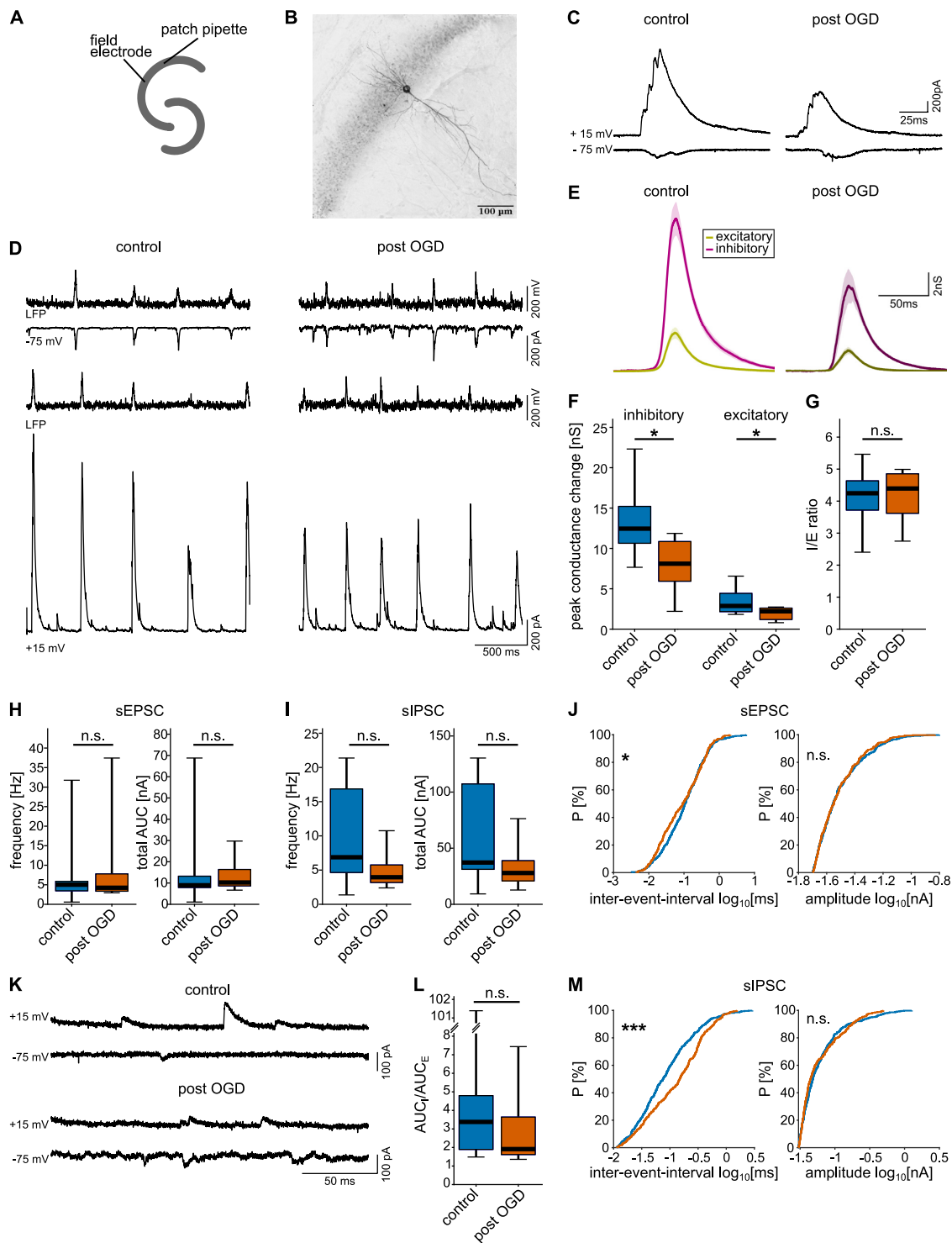
Figure 4. Whole-cell voltage-clamp recordings from CA1 PYRs yield reduced conductance changes, yet preserved network balance after OGD. **A**, Experimental design. A field electrode and a patch pipette placed in the CA1 region of the hippocampal slice, recorded in a double-perfused, submerged-style chamber. **B**, Summed view of a representative 60× confocal image z-stack of a biocytin-filled CA1 PYR from the post-OGD group. The background was removed using the rolling-ball algorithm and the LUT was inverted. **C**, Representative current traces during SPW-R, magnified from **D**, at 15- and −75-mV nominal holding voltage. **D**, Representative traces of LFP and voltage-clamp recordings at 15- and −75-mV nominal holding voltage. **E**, Mean conductance changes during SPW-R, calculated by the Borg-Graham method (for details, see Materials and Methods). Shaded regions represent the SEM. Purple, inhibitory conductance. Khaki, excitatory conductance. **F**, Peak conductance changes during SPW-R. $p_{inhibitory} =$ 0.0202, $p_{excitatory} =$ 0.0341, Student's t test. **G**, I/E ratio, calculated as peak inhibitory conductance changes divided by peak excitatory conductance changes. $p = 0.9835$, Student's t test. **H**, sEPSCs outside of SPW-Rs. Left, Frequency of sEPSCs under control

continued

(blue) or post-OGD (orange) condition. $p = 0.7076$, Student's t test. Right, Total AUC, calculated as the area of the mean synaptic current curves multiplied by the frequency. $p = 0.6574$, Student's t test. **I**, sIPSCs outside of SPW-Rs. Left, Frequency of sIPSCs. $p = 0.0875$, Student's t test. Right, Total AUC. $p = 0.1355$, Student's t test. **J**, For the cumulative distribution of sEPSC IEIs and sEPSC amplitudes, 50 data points from each cell were pooled together. Left, Cumulative distribution of sEPSC IEI. $p = 0.027$, two-sample Kolmogorov–Smirnov (KS) test. Right, Cumulative distribution of sEPSC amplitude. $p = 0.946$, two-sample KS test. **K**, Magnification of current traces in **D**, displaying sPSCs outside SPW-R. Nominal holding potential is displayed. **L**, I/E ratio of sPSC outside SPW-R was computed as AUC_I/AUC_E. $p = 0.3148$, Wilcoxon rank-sum test. **M**, For the cumulative distribution of sIPSC IEI and sIPSC amplitudes, 50 data points from each cell were pooled together. Left, Cumulative distribution of sIPSC IEI. $p = 4 \times 10^{-9}$, two-sample KS test. Right, Cumulative distribution of sIPSC amplitude. $p = 0.061$, two-sample KS test. $n_{control} = 10$ cells from 7 slices and 5 mice. $n_{post-OGD} = 7$ cells from 5 slices and the same 5 mice; *$p < 0.05$, ***$p < 0.001$; n.s., not significant.

strongly coupled to SPW-R events in both CA1 and CA3 (Fig. 5F,G). On ripple oscillations, MUA took place preferentially during the trough (0–30°) of ripple cycles, leading to an oscillatory shape of the averaged cross-correlogram (Fig. 5F,G). Following OGD, this characteristic coupling to SPW-R oscillations remained largely unaltered (Fig. 5F,G). Thus, slices appear to display deficits in the initiation of sharp waves and ripple-oscillations following transient OGD, while the characteristic SPW-R waveform and the entrainment of neuronal activity are mostly preserved.

Neurons are activated differentially by transient hypoxia depending on hippocampal subregion

So far, we observed a differential effect of transient hypoxia on electrophysiologically measured activity in different hippocampal regions and neuronal types. To further elucidate the effects of transient OGD on neuronal activation, we tested for cell death and neuronal activation across PYR and PV-IN in both CA1 and CA3. Most of the common apoptosis and stress markers reach their maximal expression within several hours after the insult, which is beyond the time window of our *in vitro* experiment. Acute cell death, however, is readily observable within short time intervals after an insult, using nuclear cross section area as a morphologic marker (Bonde et al., 2002). Additionally, co-expression of the immediate-early gene product c-Fos, known to be upregulated after hypoxic insults and spreading depression (Dragunow et al., 1990; Kiessling et al., 1993), was quantified by immunofluorescence. To these ends we performed quadruple stainings for c-Fos, PV, NeuN, and DAPI in slices that had undergone OGD and compared them to slices after control incubation (Fig. 6A,B,I,J).

There was no difference in the number of CA1 NeuN+/PV– cells or CA1 PV+ cells per area between conditions (Fig. 6C,F). The number of CA3 NeuN+/PV– cells, however, was decreased post-OGD (43.3 [37.9; 56.8] $\times 10^{-3}$ [μm^2]$^{-1}$ compared with 58.4 [47.5; 89.8] $\times 10^{-3}$ [μm^2]$^{-1}$; Fig. 6K), while the number of CA3 PV+ cells was unchanged (Fig. 6N). Neither NeuN+ nor PV+ neurons showed clear signs of necrosis after transient OGD, as the nuclear area was unchanged (Fig. 6D,G,L,O). This was the case in both the CA1 and CA3 region.

c-Fos staining revealed a differential effect of transient OGD on cellular activation. In the CA1 region the percentage of c-Fos-positive cells was increased among PV-IN from 46.2% [40.0%; 66.7%] to 62.5% [47.2%; 78.9%] ($p = 0.03$) after transient OGD while it was unchanged for NeuN+/PV– cells (Fig. 6E,H). In the CA3 region, on the other hand, the percentage of c-Fos-positive NeuN+/PV– neurons was significantly higher in slices which had undergone transient hypoxia than in controls (49.8% [40.7%; 57.9%] compared with 23.9% [17.3%; 53.2%]; $p = 0.0007$) with no change among PV-INs (Fig. 6M,P). Thus, a moderate and differentiated effect of transient OGD on c-Fos protein expression was visible.

Discussion

While cascades leading to acute necrosis and apoptosis after a severe insult are relatively well understood, knowledge about functional recovery after transient HI is still rather vague. Our data show a reduced recovery of electrophysiologal FSI activity compared with PYR combined with alterations of synchronous network events.

The vulnerability of PV+ FSI is a particularly important issue, and it is presently unclear to which extent their altered function contributes to impaired posthypoxic network activity (Johansen et al., 1983; Nitsch et al., 1989; Moga et al., 2002; Wang, 2003; Povysheva et al., 2019; Elzoheiry et al., 2020). Earlier studies found unchanged numbers of PV-IN in contrast to reduced CA1 PYR numbers several days after HI *in vivo* (Johansen et al., 1983; Nitsch et al., 1989). Calcium-binding properties of PV are discussed to reduce neurotoxic effects of calcium overload during HI (Tortosa and Ferrer, 1993). However, more recent studies indicate impaired function of inhibitory neurons compared with excitatory neurons after transient metabolic insults (Moga et al., 2002; Wang, 2003; Povysheva et al., 2019; Elzoheiry et al., 2020). It is important to note the methodical differences in those studies in terms of insult severity and outcome measures (histologic cell death vs electrophysiological function).

Our data from tetrode recordings in acute hippocampal slices are in line with those more recent reports (Povysheva et al., 2019; Elzoheiry et al., 2020), demonstrating an increased functional vulnerability of FSI compared with PYR. However, while Povysheva et al. (2019) found that PV-IN held in current-clamp during transient OGD showed no recovery of membrane potential and spiking activity, which the authors interpreted as a sign of cell death, cells remained clearly viable under our experimental conditions, but showed distinct functional deficits. In contrast to results from Elzoheiry et al. (2020), who employed a pharmacological metabolic challenge, we did not observe an overall increase in PYR activity, in line with the unaltered I/E ratio in our cellular recordings.
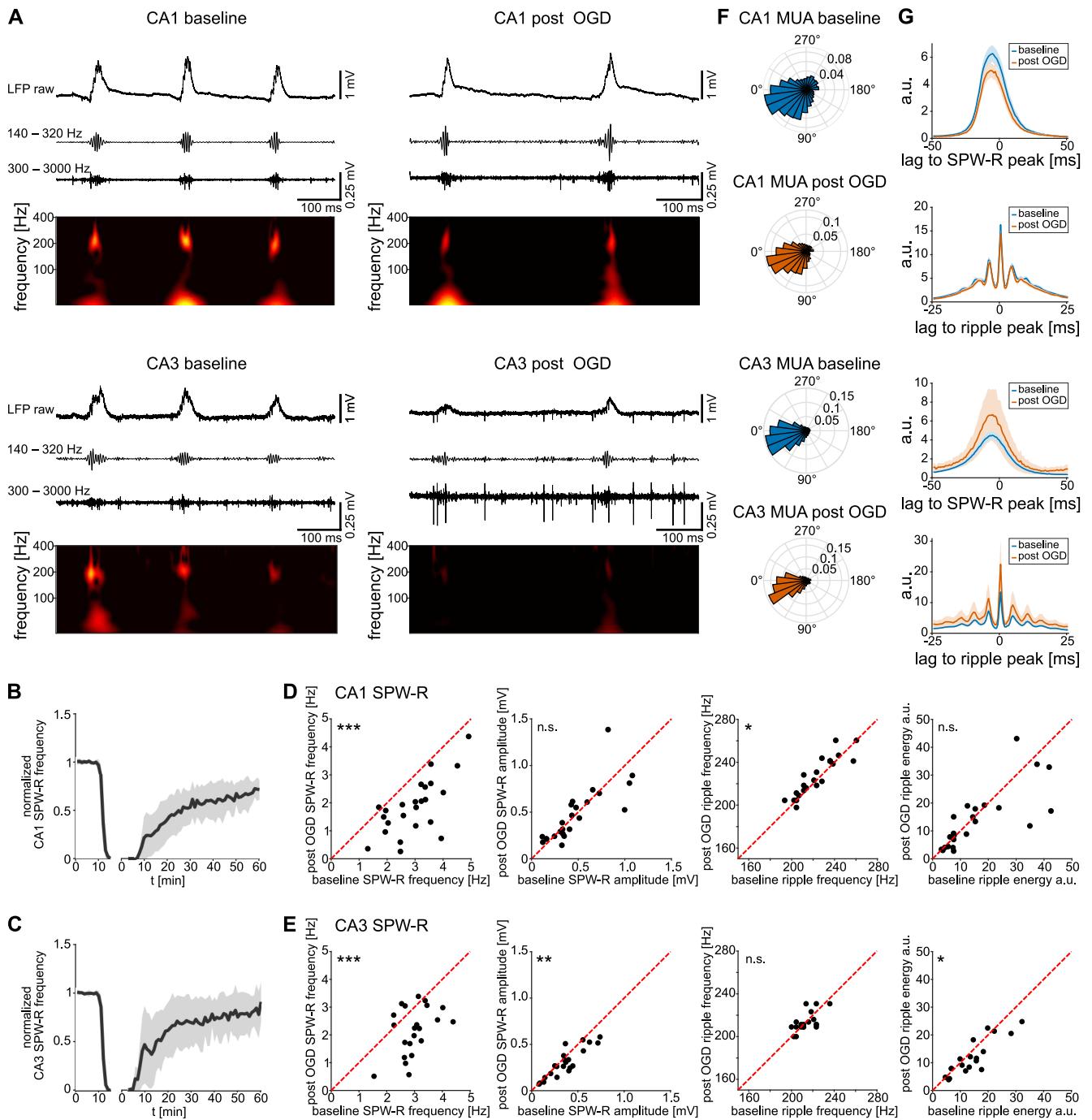
Figure 5. SPW-Rs re-emerge with reduced incidence and altered ripple properties. ***A***, Representative LFP traces, exhibiting sponta-neous SPW-R activity, recorded simultaneously from CA1 (top) and CA3 (bottom). Displayed traces, under baseline conditions (left) and after OGD (right) stem from the same recording. Below each raw trace, the corresponding bandpass filtered traces to highlight ripples (140–320 Hz) and MUA (300–3000 Hz), and the power-spectrogram are displayed. ***B***, ***C***, Binned median amplitude of SPW-R (***B***, CA1; ***C***, CA3), normalized by the median baseline amplitude. Shaded regions represent median absolute deviation. Minutes 0–10, baseline condition; minutes 10–15, OGD. Gap, HSD. Traces after gap, recovery during reperfusion. Time count on the right part of the x-axis begins with the time point of the HSD. ***D***, ***E***, SPW-R characteristics (***D***, CA1; ***E***, CA3). From right to left, SPW-R inci-dence, $p_{CA1} = 3 \times 10^{-7}$, $p_{CA3} = 0.0001$; SPW-R amplitude, $p_{CA1} = 0.9624$, $p_{CA3} = 0.0024$; ripple frequency, $p_{CA1} = 0.0465$, $p_{CA3} = 0.8371$; ripple energy, $p_{CA1} = 0.2403$, $p_{CA3} = 0.0112$. Student's paired t test. ***F***, Phase plot of MUA on ripples from a representative recording, normalized by spike probability. ***G***, Mean cross-correlation between SPW-R peaks and MUA spikes (first and third graph), and mean cross-correlation between ripple peaks and MUA spikes (second and fourth graphs) during baseline (blue) and post-OGD (orange) conditions. Top two graphs, CA1. Bottom two graphs, CA3. Shaded regions represent the SEM. Correlations were normalized, as follows: $n_{norm} = n_{corr}/\text{sqrt}(n_{ev1} \times n_{ev2})$. $n_{CA1} = 24$ slices from 12 mice, $n_{CA3} = 22$ slices from 12 mice; *$p < 0.05$, **$p < 0.01$, ***$p < 0.001$; n.s., not significant.
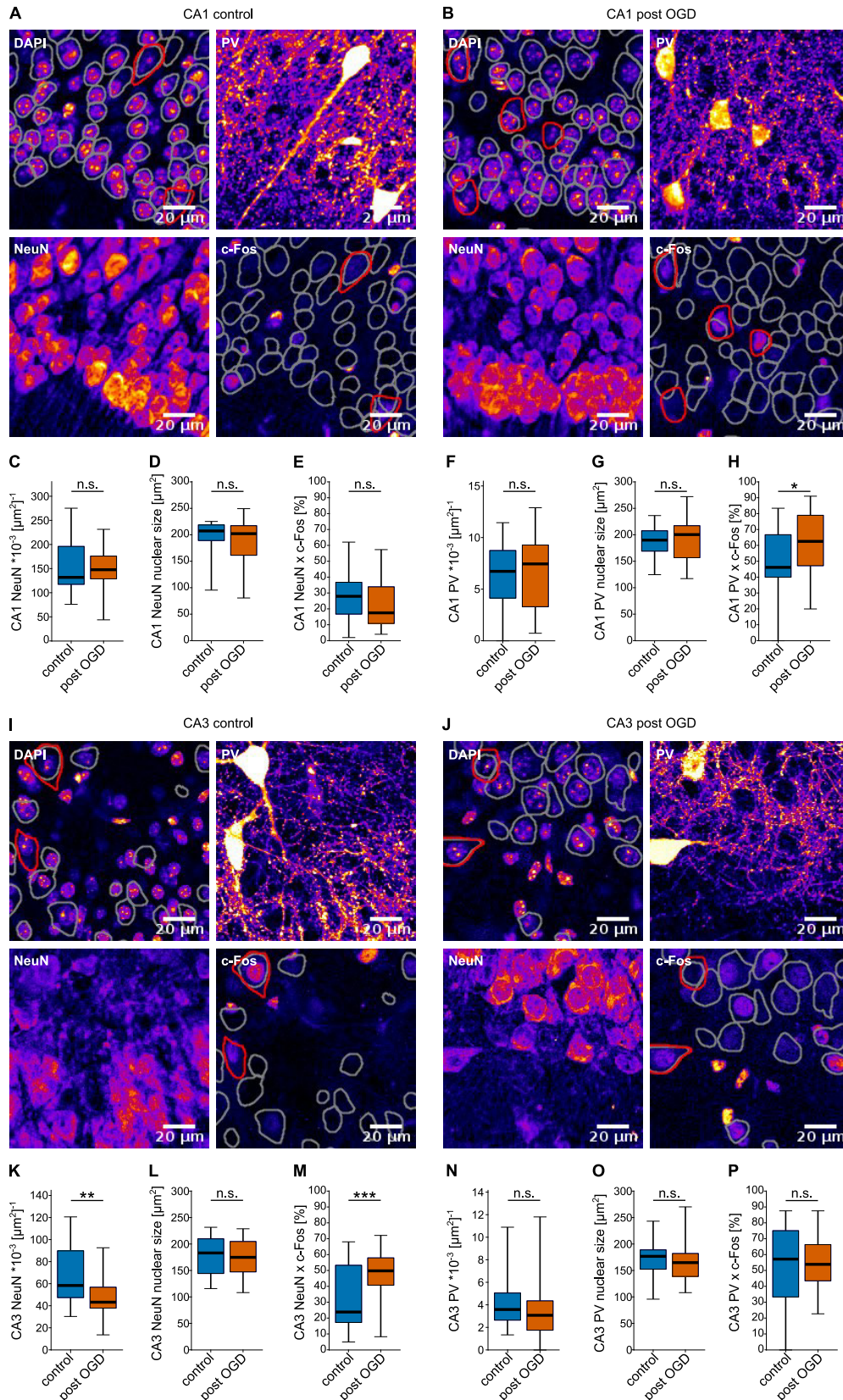
Figure 6. Altered c-Fos expression after OGD depends on region and cell type. *A*, *B*, *I*, *J*, Fire-LUT of representative four-channel confocal images of the CA1 (*A*, *B*) and CA3 (*I*, *J*) region in quadrupel-stained hippocampal slices at 20× magnification after background removal with the rolling-ball algorithm. Channels are indicated in the top left corner of each image. In the c-Fos and DAPI

continued

channel gray and red overlays denote NeuN+ and PV+ cell outlines as determined by the cellpose algorithm, respectively. ***C***, Number of NeuN+ cells per 1000 μm^2 in CA1. $p = 0.5846$. ***D***, Nuclear area of NeuN+ neurons in CA1. $p = 0.4262$. ***E***, Percentage of NeuN+/PV− neurons co-expressing c-Fos in CA1. $p = 0.0995$. ***F***, Number of PV+ cells per 1000 μm^2 in CA1. $p = 0.5702$. ***G***, Nuclear area of PV+ neurons in CA1. $p = 0.833$. ***H***, Percentage of PV+ neurons co-expressing c-Fos in CA1. $p = 0.0305$, Student's *t* test. ***K***, Number of NeuN+ cells per 1000 μm^2 in CA3. $n_{control} = 26$, $n_{post-OGD} = 34$. $p = 0.0016$. ***L***, Nuclear area of NeuN+ neurons in CA3. $p = 0.6601$. ***M***, Percentage of NeuN+/PV− neurons co-expressing c-Fos in CA3. $p = 0.0007$. ***N***, Number of PV+ cells per 1000 μm^2 in CA3. $n_{control} = 26$, $n_{post-OGD} = 34$. $p = 0.1363$. ***O***, Nuclear area of PV+ neurons in CA3. $p = 0.5933$. ***P***, Percentage of PV+ neurons co-expressing c-Fos in CA3. $p = 0.7764$. $n_{control} = 26$ slices from 7 animals, $n_{post-OGD} = 34$ slices from 7 animals (for cell marker counts). $n_{CA1\ control} = 25$ slices from 7 animals, $n_{CA1\ post-OGD} = 28$ slices from 7 animals, $n_{CA3\ control} = 22$ slices from 7 animals, $n_{CA3\ post-OGD} = 23$ slices from 7 animals (for DAPI and c-Fos co-expression, slices with less than five PV-IN in the ROI were excluded); $*p < 0.05$, $**p < 0.01$, $***p < 0.001$; n.s., not significant. Student's *t* test.

Results from tetrode-recorded putative FSI are consistent with data from cell-attached recordings from PV-IN in CA1, both showing a reduction of overall spiking frequency of ∼60%. While excitatory feedback from PYR to PV-IN drives their activity and stabilizes of neuronal ensembles (Cornford et al., 2019), this result cannot be explained by diminished excitatory drive alone as the reduction of PV-IN spiking by far exceeds the reduction of PYR activity. Several implications may arise from this reduced FSI activity: (1) a relative lack of inhibition is expected to lead to decreased I/E ratios, which may even result in increased activity of PYRs and, in the extreme case, epileptic seizures (Stief et al., 2007); (2) a loss of precisely timed phasic inhibition by FSI might impair temporal cell-to-network coupling and thereby reduce ripple-associated spike timing (Gan et al., 2017); and (3) altered reciprocal interaction between FSI and PYR could affect the generation of SPW-R activity (Schlingloff et al., 2014).

OGD led to similarly decreased inhibitory and excitatory conductance changes in CA1 PYR during SPW-R. As a result, I/E ratio during SPW-R remained largely unaltered. This finding seems to be at odds with the observed stronger reduction in FSI firing frequency as compared with PYR. One possible explanation would be that a sufficiently high I/E ratio may be a precondition for the occurrence of SPW-R (Hájos et al., 2013; Schlingloff et al., 2014), such that SPW-Rs occur less frequently, but, once generated, show a near-normal I/E value. We therefore examined sPSCs in-between SPW-R. Here, sIPSCs, but not sEPSCs, exhibited increased IEI. This would suggest reduced inhibition; the I/E ratio, however, was not significantly altered. Thus, subtle differences in neuronal behavior can be observed depending on network state after recovery from OGD, while the relative deficiency in fast inhibition is not accompanied by a drastic increase of the excitatory drive onto PYR. This is relevant, as it largely excludes a potentiation of excitotoxic processes triggered by HI during the acute recovery phase.

Additionally, in none of our experiments epileptiform or ictal-like events occurred, showing that in our relatively mild HI model a sufficient level of tonic inhibition remains after OGD. The insult severity in our study thus rather resembles the relatively mild transient ischemic attacks, which are far less linked to epilepsy than a full stroke (Arntz et al., 2013).

Homeostatic mechanisms may compensate for the lower frequency of discharges in PV-IN (Turrigiano et al., 1998). This may include increased quantal content of IPSCs, in line with the largely unaltered amplitude of spontaneous inhibitory currents, or even changes in quantal size (Hartmann et al., 2008), which were not measured in the present study. Also, non-PV interneurons innervating PYR may partially compensate for the loss of activity on PV-IN, such that the overall balance between excitation and inhibition was preserved, although PV-IN constitute the class thought to be most relevant to SPW-R (Klausberger and Somogyi, 2008). As a result, we did not observe overt hyperexcitability of PYR.

In contrast, PYR firing frequency was reduced and their temporal coupling to the network was preserved. Of course, further mechanisms may contribute to the behavior of PYR post-OGD. Increased firing may result from the reduction of inhibition (Elzoheiry et al., 2020), increased excitability (Fan et al., 2008), and ischemic long-term potentiation (Maggio et al., 2015). On the other hand, factors like the lack of energy-producing metabolites following hypoxia (Kass and Lipton, 1989), perturbed neuronal ion homeostasis (Müller and Somjen, 2000), and calcium-triggered disruption of the axon-initial segment morphology (Revah et al., 2019) may reduce neuronal activity following OGD and HSD.

As both FSI and PYR activity is entrained by SPW-R oscillations, network interactions have a major influence on the results of this study. Future studies with other experimental designs are required to investigate intrinsic factors of FSI vulnerability and their functional outcome in the context of other network states.

As has been shown previously (Hefter et al., 2016), SPW-Rs were transiently abolished during OGD, but re-emerged shortly after reperfusion. Spontaneous network oscillations partially recovered in all slices and their overall waveform, consisting of slow large-amplitude sharp waves and superimposed high-frequency ripples, was maintained. However, several subtle, region-specific changes could be observed. Reduced incidence of SPW-R in both CA3 and CA1 indicates impaired generation of oscillatory activity following OGD. While the exact mechanism of SPW-R generation is still debated, activation of FSI by PYR is a critical part. It has been shown that FSI firing is associated with succeeding SPW-R (Bazelot et al., 2016). During SPW-R, hippocampal neurons repeatedly fire in specific patterns and on a certain phase of the ripple cycle (Reichinnek et al., 2010). This replay is thought to be pivotal for consolidation of episodic and special memory in the hippocampus (van de Ven et al., 2016). As discussed above, reduced SPW-R oscillations may hint toward impaired interplay between FSI and PYRs.

In contrast to CA1, SPW-R amplitude and ripple energy were reduced in CA3 after reperfusion, indicating that either less CA3 neurons or smaller PSCs contribute to the LFP signature of these oscillations after OGD. On the other hand, these smaller CA3 SPW-R still seem to be sufficient to elicit SPW-R of unaltered magnitude in CA1. These networks appear to be less affected by OGD than those in CA3, possibly because of reduced inhibitory control or to hypoxia-triggered plastic effects such as ischemic LTP (Crepel et al., 2003). A subtle increase in ripple frequency can be observed in CA1, possibly indicating a smaller ensemble size contributing to these oscillations. Intact hippocampo-neocortical connectivity is considered crucial for memory and executive function (Girardeau et al., 2009; Sigurdsson and Duvarci, 2016). Reduced output of SPW-R from CA1 might impair these connections and thus cognitive function.

PV-IN firing is strongly coupled to SPW-R and reaches frequencies around 200 Hz in cell-attached recording. Notably, the observed reduction of PV-IN frequency mostly results from reduced firing on SPW-R, while spiking outside of SPW-R is unaltered. The reduction of phasic inhibition seems to be remarkably well compensated, having quite little impact on the precisely timed network function.

Our histologic data largely exclude that the observed functional alterations are explained by cell death, as the absence of nuclear shrinkage in our data indicates that no significant amount of cell death occurred (Bonde et al., 2002). Nuclear shrinkage could be a sign of either beginning apoptosis or necrosis, while most common markers of these processes are not upregulated at the short time scale of the experiment. The apparent absence of dying cells was expected because of the short duration of the OGD insult. This notion is also in line with the fact that most (>95%) identified units re-appeared after the OGD (Fig. 1D). However, it cannot be excluded that cell death would have occurred beyond our experimental time window of ~1 h after OGD. Indeed, hippocampal neurons are known to undergo delayed apoptosis 24–72 h after HI (Kirino, 2000). The surprising reduction in CA3 NeuN+/PV– cells most likely does not indicate cell death but could be a sign of postischemic cellular damage (Ûnal-Çevik et al., 2004). This would be in line with the strong effect of transient OGD on CA3 network oscillations compared with CA1, hinting toward a reduced size of the recruited ensembles. The unchanged number of detected PV+ cells indicates that a full depletion of intracellular PV in its capacity as a calcium buffer did not take place and is not the main mechanism behind PV-IN dysfunction in our experiment, in line with the "interneuron energy hypothesis" (Kann, 2016).

Furthermore, we stained for the transcription factor c-Fos in PV+ and NeuN+/PV– cells (which are comprised almost exclusively of PYR in the PYR layer). c-Fos serves as an activity marker and is known to be upregulated early after HI (Kiessling et al., 1993). The c-Fos staining revealed regional differences between PV+ and PYR neurons after OGD. While OGD led to an increase of c-Fos+/PV+ cells in CA1, in CA3 c-Fos+ PYR increased. The observed levels of c-Fos expression are comparable to measurements after brief transient HI in vivo (Kiessling et al., 1993).

In summary, our study supports the hypothesis that FSI are functionally more vulnerable to HI insults as compared with PYR. However, in our experimental paradigm, the I/E balance after reperfusion was not significantly perturbed and the main features of SPW-R oscillations and cell-to-LFP coupling were maintained. Nonetheless, the distinct, region-specific alterations in SPW-R activity, which arose after recovery, implicate impaired information processing in the hippocampus. Impaired generation of SPW-R as observed in our study implicates scarcer information replay and thus might hamper memory consolidation. Treatments aiming to protect or restore the inhibitory function of FSI might improve network function after cerebral HI and prevent the development of lasting functional deficits.

References

Aitken PG, Schiff SJ (1986) Selective neuronal vulnerability to hypoxia in vitro. Neurosci Lett 67:92–96.

Arntz R, Rutten-Jacobs L, Maaijwee N, Schoonderwaldt H, Dorresteijn L, van Dijk E, de Leeuw F-E (2013) Post-stroke epilepsy in young adults: a long-term follow-up study. PLoS One 8:e55498.

Bazelot M, Teleńczuk MT, Miles R (2016) Single CA3 pyramidal cells trigger sharp waves in vitro by exciting interneurones. J Physiol 594:2565–2577.

Bonde C, Noraberg J, Zimmer J (2002) Nuclear shrinkage and other markers of neuronal cell death after oxygen–glucose deprivation in rat hippocampal slice cultures. Neurosci Lett 327:49–52.

Borg-Graham LJ, Monier C, Frégnac Y (1998) Visual input evokes transient and strong shunting inhibition in visual cortical neurons. Nature 393:369–373.

Both M, Bähner F, von Bohlen und Halbach O, Draguhn A (2008) Propagation of specific network patterns through the mouse hippocampus. Hippocampus 18:899–908.

Broughton BRS, Reutens DC, Sobey CG (2009) Apoptotic mechanisms after cerebral ischemia. Stroke 40:e331–e339.

Buzsáki G (2015) Hippocampal sharp wave-ripple: a cognitive biomarker for episodic memory and planning. Hippocampus 25:1073–1188.

Buzsáki G, Draguhn A (2004) Neuronal oscillations in cortical networks. Science 304:1926–1929.

Chaure FJ, Rey HG, Quian Quiroga R (2018) A novel and fully automatic spike-sorting implementation with variable number of features. J Neurophysiol 120:1859–1871.

Cornford JH, Mercier MS, Leite M, Magloire V, Häusser M, Kullmann DM (2019) Dendritic NMDA receptors in parvalbumin neurons enable strong and stable neuronal assemblies. Elife 8:e49872.

Crepel V, Epsztein J, Ben-Ari Y (2003) Ischemia induces short- and long-term remodeling of synaptic activity in the hippocampus. J Cell Mol Med 7:401–407.

Croning MDR, Haddad GG (1998) Comparison of brain slice chamber designs for investigations of oxygen deprivation in vitro. J Neurosci Methods 81:103–111.

Csicsvari J, Hirase H, Czurkó A, Mamiya A, Buzsáki G (1999) Oscillatory coupling of hippocampal pyramidal cells and interneurons in the behaving rat. J Neurosci 19:274–287.

Dragunow M, Goulding M, Faull RLM, Ralph R, Mee E, Frith R (1990) Induction of c-fos mRNA and protein in neurons and glia after traumatic brain injury: pharmacological characterization. Exp Neurol 107:236–248.

Dreier JP (2011) The role of spreading depression, spreading depolarization and spreading ischemia in neurological disease. Nat Med 17:439.

Elzoheiry S, Lewen A, Schneider J, Both M, Hefter D, Boffi JC, Hollnagel JO, Kann O (2020) Mild metabolic stress is sufficient to disturb the formation of pyramidal cell ensembles during gamma oscillations. J Cereb Blood Flow Metab 40:2401–2415.

English DF, McKenzie S, Evans T, Kim K, Yoon E, Buzsáki G (2017) Pyramidal cell-interneuron circuit architecture and dynamics in hippocampal networks. Neuron 96:505–520.e7.

Fan Y, Deng P, Wang YC, Lu HC, Xu ZC, Schulz PE (2008) Transient cerebral ischemia increases CA1 pyramidal neuron excitability. Exp Neurol 212:415–421.

Gan J, Weng S, Pernía-Andrade AJ, Csicsvari J, Jonas P (2017) Phase-locked inhibition, but not excitation, underlies hippocampal ripple oscillations in awake mice in vivo. Neuron 93:308–314.

GBD 2019 Diseases and Injuries Collaborators (2020) Global burden of 369 diseases and injuries in 204 countries and territories, 1990–2019: a systematic analysis for the Global Burden of Disease Study 2019. Lancet 396:1204–1222.

Girardeau G, Benchenane K, Wiener SI, Buzsáki G, Zugaro MB (2009) Selective suppression of hippocampal ripples impairs spatial memory. Nat Neurosci 12:1222–1223.

Guggisberg AG, Koch PJ, Hummel FC, Buetefisch CM (2019) Brain networks and their relevance for stroke rehabilitation. Clin Neurophysiol 130:1098–1124.

Haider B, Duque A, Hasenstaub AR, McCormick DA (2006) Neocortical network activity in vivo is generated through a dynamic balance of excitation and inhibition. J Neurosci 26:4535–4545.

Hainmueller T, Bartos M (2018) Parallel emergence of stable and dynamic memory engrams in the hippocampus. Nature 558:292–296.

Hájos N, Ellender TJ, Zemankovics R, Mann EO, Exley R, Cragg SJ, Freund TF, Paulsen O (2009) Maintaining network activity in submerged hippocampal slices: importance of oxygen supply. Eur J Neurosci 29:319–327.

Hájos N, Karlócai MR, Németh B, Ulbert I, Monyer H, Szabó G, Erdélyi F, Freund TF, Gulyás AI (2013) Input-output features of anatomically identified CA3 neurons during hippocampal sharp wave/ripple oscillation in vitro. J Neurosci 33:11677–11691.

Hartmann K, Bruehl C, Golovko T, Draguhn A (2008) Fast homeostatic plasticity of inhibition via activity-dependent vesicular filling. PLoS One 3:e2979.

Hefter D, Kaiser M, Weyer SW, Papageorgiou IE, Both M, Kann O, Müller UC, Draguhn A (2016) Amyloid precursor protein protects neuronal network function after hypoxia via control of voltage-gated calcium channels. J Neurosci 36:8356–8371.

Huchzermeyer C, Berndt N, Holzhütter HG, Kann O (2013) Oxygen consumption rates during three different neuronal activity states in the hippocampal CA3 network. J Cereb Blood Flow Metab 33:263–271.

Ishizuka N, Weber J, Amaral DG (1990) Organization of intrahippocampal projections originating from CA3 pyramidal cells in the rat. J Comp Neurol 295:580–623.

Johansen FF, Balslev Jørgensen M, Diemer NH (1983) Resistance of hippocampal CA-1 interneurons to 20 min of transient cerebral ischemia in the rat. Acta Neuropathol 61:135–140.

Kann O (2012) The energy demand of fast neuronal network oscillations: insights from brain slice preparations. Front Pharmacol 2:90.

Kann O (2016) The interneuron energy hypothesis: implications for brain disease. Neurobiol Dis 90:75–85.

Kann O, Papageorgiou IE, Draguhn A (2014) Highly energized inhibitory interneurons are a central element for information processing in cortical networks. J Cereb Blood Flow Metab 34:1270–1282.

Kass IS, Lipton P (1989) Protection of hippocampal slices from young rats against anoxic transmission damage is due to better maintenance of ATP. J Physiol 413:1–11.

Kiessling M, Stumm G, Xie Y, Herdegen T, Aguzzi A, Bravo R, Gass P (1993) Differential transcription and translation of immediate early genes in the gerbil hippocampus after transient global ischemia. J Cereb Blood Flow Metab 13:914–924.

Kirino T (2000) Delayed neuronal death. Neuropathology 20 [Suppl]: S95–S97.

Klausberger T, Somogyi P (2008) Neuronal diversity and temporal dynamics: the unity of hippocampal circuit operations. Science 321:53–57.

Lee SH, Marchionni I, Bezaire M, Varga C, Danielson N, Lovett-Barron M, Losonczy A, Soltesz I (2014) Parvalbumin-positive basket cells differentiate among hippocampal pyramidal cells. Neuron 82:1129–1144.

Maggio N, Shavit Stein E, Segal M (2015) Ischemic LTP: NMDA-dependency and dorso/ventral distribution within the hippocampus. Hippocampus 25:1465–1471.

Maier N, Morris G, Johenning FW, Schmitz D (2009) An approach for reliably investigating hippocampal sharp wave-ripples in vitro. PLoS One 4:e6925.

Maier P, Kaiser ME, Grinevich V, Draguhn A, Both M (2016) Differential effects of oxytocin on mouse hippocampal oscillations in vitro. Eur J Neurosci 44:2885–2898.

Mattson MP, Culmsee C, Yu ZF (2000) Apoptotic and antiapoptotic mechanisms in stroke. Cell Tissue Res 301:173–187.

Moga D, Hof PR, Vissavajjhala P, Moran TM, Morrison JH (2002) Parvalbumin-containing interneurons in rat hippocampus have an AMPA receptor profile suggestive of vulnerability to excitotoxicity. J Chem Neuroanat 23:249–253.

Müller M, Somjen GG (2000) Na(+) and K(+) concentrations, extra- and intracellular voltages, and the effect of TTX in hypoxic rat hippocampal slices. J Neurophysiol 83:735–745.

Nimmrich V, Maier N, Schmitz D, Draguhn A (2005) Induced sharp wave-ripple complexes in the absence of synaptic inhibition in mouse hippocampal slices. J Physiol 563:663–670.

Nitsch C, Scotti A, Sommacal A, Kalt G (1989) GABAergic hippocampal neurons resistant to ischemia-induced neuronal death contain the Ca2+-binding protein parvalbumin. Neurosci Lett 105:263–268.

Pendlebury ST, Rothwell PM (2009) Prevalence, incidence, and factors associated with pre-stroke and post-stroke dementia: a systematic review and meta-analysis. Lancet Neurol 8:1006–1018.

Perkins KL (2006) Cell-attached voltage-clamp and current-clamp recording and stimulation techniques in brain slices. J Neurosci Methods 154:1–18.

Povysheva N, Nigam A, Brisbin AK, Johnson JW, Barrionuevo G (2019) Oxygen–glucose deprivation differentially affects neocortical pyramidal neurons and parvalbumin-positive interneurons. Neuroscience 412:72–82.

Quiroga RQ, Nadasdy Z, Ben-Shaul Y (2004) Unsupervised spike detection and sorting with wavelets and superparamagnetic clustering. Neural Comput 16:1661–1687.

Reichinnek S, Künsting T, Draguhn A, Both M (2010) Field potential signature of distinct multicellular activity patterns in the mouse hippocampus. J Neurosci 30:15441–15449.

Revah O, Stoler O, Neef A, Wolf F, Fleidervish IA, Gutnick MJ (2019) Dynamic gain analysis reveals encoding deficiencies in cortical neurons that recover from hypoxia-induced spreading depolarizations. J Neurosci 39:7790–7800.

Schindelin J, Arganda-Carreras I, Frise E, Kaynig V, Longair M, Pietzsch T, Preibisch S, Rueden C, Saalfeld S, Schmid B, Tinevez JY, White DJ, Hartenstein V, Eliceiri K, Tomancak P, Cardona A (2012) Fiji: an open-source platform for biological-image analysis. Nat Methods 9:676–682.

Schlingloff D, Kali S, Freund TF, Hajos N, Gulyas AI (2014) Mechanisms of sharp wave initiation and ripple generation. J Neurosci 34:11385–11398.

Schmidt-Kastner R (2015) Genomic approach to selective vulnerability of the hippocampus in brain ischemia–hypoxia. Neuroscience 309:259–279.

Schmidt-Kastner R, Freund TF (1991) Selective vulnerability of the hippocampus in brain ischemia. Neuroscience 40:599–636.

Schönberger J, Draguhn A, Both M (2014) Lamina-specific contribution of glutamatergic and GABAergic potentials to hippocampal sharp wave-ripple complexes. Front Neural Circuits 8:103.

Schurr A, Rigor BM (1989) Cerebral ischemia revisited: new insights as revealed using in vitro brain slice preparations. Experientia 45:684–695.

Şekerdağ E, Solaroğlu I, Gürsoy-Özdemir Y (2018) Cell death mechanisms in stroke and novel molecular and cellular treatment options. Curr Neuropharmacol 16:1396–1415.

Sigurdsson T, Duvarci S (2016) Hippocampal-prefrontal interactions in cognition, behavior and psychiatric disease. Front Syst Neurosci 9:190.

Sirota A, Montgomery S, Fujisawa S, Isomura Y, Zugaro M, Buzsáki G (2008) Entrainment of neocortical neurons and gamma oscillations by the hippocampal theta rhythm. Neuron 60:683–697.

Somjen GG (2001) Mechanisms of spreading depression and hypoxic spreading depression-like depolarization. Physiol Rev 81:1065–1096.

Stief F, Zuschratter W, Hartmann K, Schmitz D, Draguhn A (2007) Enhanced synaptic excitation–inhibition ratio in hippocampal interneurons of rats with temporal lobe epilepsy. Eur J Neurosci 25:519–528.

Stringer C, Wang T, Michaelos M, Pachitariu M (2021) Cellpose: a generalist algorithm for cellular segmentation. Nat Methods 18:100–106.

Tortosa A, Ferrer I (1993) Parvalbumin immunoreactivity in the hippocampus of the gerbil after transient forebrain ischaemia: a qualitative and quantitative sequential study. Neuroscience 55:33–43.

Turrigiano GG, Leslie KR, Desai NS, Rutherford LC, Nelson SB (1998) Activity-dependent scaling of quantal amplitude in neocortical neurons. Nature 391:892–896.

Ûnal-Çevik I, Kılınç M, Gürsoy-Özdemir Y, Gurer G, Dalkara T (2004) Loss of NeuN immunoreactivity after cerebral ischemia does not indicate neuronal cell loss: a cautionary note. Brain Res 1015:169–174.

van de Ven GM, Trouche S, McNamara CG, Allen K, Dupret D (2016) Hippocampal offline reactivation consolidates recently formed cell assembly patterns during sharp wave-ripples. Neuron 92:968–974.

Wang JH (2003) Short-term cerebral ischemia causes the dysfunction of interneurons and more excitation of pyramidal neurons in rats. Brain Res Bull 60:53–58.

Ylinen A, Bragin A, Nadasdy Z, Jando G, Szabo I, Sik A, Buzsaki G (1995) Sharp wave-associated high-frequency oscillation (200 Hz) in the intact hippocampus: network and intracellular mechanisms. J Neurosci 15:30–46.